A
Thesis on

Optical and Dielectric studies of La doped $BiFeO_3$

Dissertation submitted in partial fulfilment for the requirement of the award of the degree of

Master of Technology
In
Materials and Metallurgical Engineering

Under
The supervision of
Dr. Poonam Uniyal
(Assistant Professor)

Submitted by
Shashank Sharma
Roll no: - 601102010

School of Physics and Materials Science
Thapar University
Patiala (Punjab) – 147004
July, 2013

Certificate

This is to certify that the thesis entitled **"Optical and Dielectric studies of La doped $BiFeO_3$"** *submitted by* ***Mr. Shashank Sharma*** *in the partial fulfillment of the requirement for the award of the degree of Master of Technology in Materials And Metallurgical Engineering from the School of Physics and Materials Science, Thapar University, Patiala, is an authentic record of his own work carried out under the supervision and guidance of* ***Dr. Poonam Uniyal****. The matter embodied in this report is one of the candidate's own record and not submitted to any other university in any part or full form for the award of such kind of degree.*

Dr. Poonam Uniyal

Supervisor

(Assistant professor)

School of Physics and Materials Science

Thapar University

Patiala, Punjab

Countersigned By:

(Dr. Kulvir Singh)

Professor and Head

School of Physics and Materials Science

Thapar University

Patiala, Punjab

(Dr. S. K. Mohapatra)

Dean Academic Affairs

Thapar University

Patiala, Punjab

Acknowledgment

First of all I would like to extend my gratitude towards my supervisor, Dr. Poonam Uniyal (Assistant Professor), School of Physics and Materials Science, Thapar University, Patiala, for giving me a chance to work in her supervision and without her help & constant guidance this thesis would have not completed.

I wish my sincere thanks to Dr. Kulvir Singh (Professor and Head), School of Physics and Materials Science, Thapar University, Patiala, who always took keen interest in guiding me during my work.

I would also like to thank Dr. N. K. Verma (Sr. Professor) School of Physics and Materials Science, Thapar University, Patiala, for providing the laboratory facility and encouragement.

I would also like to thank Dr. Manoj Kumar (Astt. Professor Jaypee Institute of Information Technology, Noida) for dielectric measurement. I am grateful to him for sharing his time and expertise.

I am also grateful to Mr. G. S. Lotey & Ms. Manpreet Kaur (Research Scholars) School of Physics and Materials Science, for their encouragement and execution of report work and providing me invaluable support and training in various techniques and uses of equipments.

I would also like to thank all the staff members of School of Physics and Materials Science for their support and encouragement.

I would also like to thank my parents, my brother and especially my beloved wife and son Kanha for their all kind of support, encouragement and blessings.

I am also very thankful to all my friends for their motivation and huge support.

Shashank Sharma

Shashank Sharma

List of Figures and Tables

List of Symbols

θ	Angle
A	Area
C	Curie constant
T_c	Curie temperature
K	Kelvin temprature
d	Interplanar Distance
E	Electric Field
n	Integer
$\prod$	Pyroelectric coefficient
P	Polarization
ε	Permittivity of material
ε_o	Permittivity of vacuum
P_r	Remnant polarization
ε_r	Relative permittivity
Ps	Spontaneous polarization
P_{sat}	Saturation value
T	Temperature
t	Thickness
λ	Wavelength
M	Mgnetization
H	Applied magnetic feild
α	Angle (lattice parameter)
Å	Angstrom
μ	Micron
β	Full width at half amxima

Abstract

Polycrystalline samples of La modified Bismuth Ferrite (Bi_{1-x} La_x FeO_3) with different compositions; x=0.0, 0.1, and 0.2 were prepared by the wet chemical route viz. Sol Gel Autocombustion method. XRD studies clearly showed the formation of rhombohedral phase for undoped $BiFeO_3$. With the increase in La concentration, the crystal structure showed transformation to orthorhombic. From the absorption spectra the band gap of nanoparticles were calculated and found to be dependent upon La-content. Frequency dependence of dielectric constant and dielectric loss in the range of 10 Hz to 1 MHz was studied at room temperature. High temperature dielectric studies showed a decrease in antiferromagnetic Neél temperature with increase in La content.

Contents

Chapter - 1 Introduction to Multiferroics

Chapter -2 Literature Review

Chapter – 3 Synthesis and Characterization Techniques

Chapter – 4 Results and Discussion

Chapter – 5 Conclusions

References

CHAPTER-1

1.1 HISTORY

The relation between electricity and magnetism has always been the keen interest of scientists and engineers. Hans Christian Oersted in 1820, observed this relationship as the magnetic compass needle deflected when he switched the current on or off in the nearby battery.

The observation made by Oersted was later on worked out by Michael Faraday, Ampère, André Marie and in 1860, James Maxwell, gave his equations, combining electricity and magnetism into one common discipline, which was, earlier, considered separately due to the reason – that electric charges of ions and electrons are responsible for charge effect and magnetic properties are governed by electron spins. However, there are cases, where these two couple strongly. For example, in the new, large field of spintronics, the effects of spins on the transport properties of solids (and vice versa) allow the possibility to control one by the other.

Strong coupling of magnetic and electric degrees of freedom in insulators can be traced back to Pierre Curie, after discovery of ferroelectricity, by Valasek, in 1920, in Rochelle Salt, but the real beginning of this field started in 1959, ie. two more phenomena, which, in principle, could exist. One is piezomagnetism, which consists of linear coupling between a magnetic field in a solid and a deformation (analogous to piezoelectricity). The other is a linear coupling between magnetic and electric fields in a media, which would cause, for example, a magnetization proportional to an electric field. Both these phenomena could exist for certain classes of magnetocrystalline symmetry.

Later on Dzyaloshinskii predicted [1], and Astrov observed [2], this type of coupling, which is now known as the linear magnetoelectric effect. This was rapidly followed by the discovery of many other compounds of this class and by a rather complete classification of possible symmetry groups allowing for the effect.

1.2 INTRODUCTION

The different types of materials possesses different types of properties broadly classified as electrical, magnetic, optical, etc., but when some of the materials show switching of these properties they are considered into a new class of materials called ferroics.

Ferroics:- A ferroic is a material that adopts a spontaneous, switchable internal alignment [3].

There are different types of ferroics:-

Ferromagnetic:- the alignment of electron spins can be switched by a magnetic field;

Ferroelectric:- electric dipole-moment alignment can be switched by an electric field; and

Ferroelastic:- strain alignment can be switched by a stress field.

1.3 MULTIFERROICS

Strong cross-coupling of responses exist in solids (i.e., the appearance of magnetization M in an electric field E, or the inverse effect of electric polarization P generated by the application of magnetic field H), there may exist systems in which two types of ordering—ferromagnetism, the spontaneous ordering of orbital and spin magnetic moments, and ferroelectricity, the spontaneous ordering of electric dipole moments—can coexist in one material in the absence of external electric and magnetic fields, these materials are now called multiferroics.

Definition by Schmid:- two or more of the primary ferroic properties are united in the same phase [4].

i). Boracites were probably the first known multiferroics [5], and soon several others were either found in nature, or synthesized artificially [6].

ii). $BiFeO_3$, $TbMnO_3$, $TbMn_2O_5$ etc are some of the examples of multiferroics.

1.3.1 Types of Multiferroics:

Multiferroics can be broadly classified into following two types [7].

i). Multiferroics of Type-I.

ii). Multiferroics of Type-II.

1.3.1.1 Multiferroics of Type I:

In these types of multiferroics magnetism and ferroelectricity have different source and appear largely independently of one another, though there is some coupling between them. These are often good ferroelectrics, and the critical temperatures of the magnetic and ferroelectric transitions can be well above room temperature. The coupling between magnetism and ferroelectricity in these materials is usually rather weak. In these materials, ferroelectricity typically appears at higher temperatures than magnetism, and the spontaneous polarization P is often rather large (of order $10 - 100\ \mu C/cm^2$).

Examples:

i). $BiFeO_3$ (T_{FE}~1100K, T_N= 643 K, P ~ 90μC/cm^2)

ii).$YMnO_3$ (T_{FE}~ 914K, T_N = 76 K, P ~ 6μC/cm^2)

There are several subclasses of type-I multiferroic but major subclasses are as follows:-

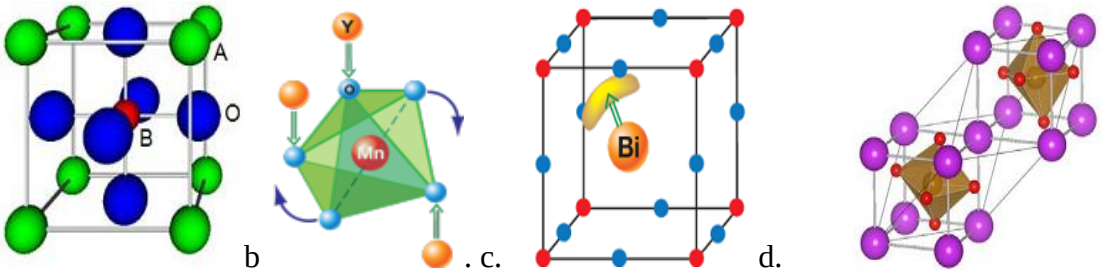

a. b . c. d.

Fig.1.1 a. Schematic view of the perovskite oxide structure, b. "Geometric" mechanism of generation of polarization in $YMnO_3$ [8], c. In $BiFeO_3$ the ordering of lone pair of Bi^{3+} ion, contributes to the polarization, d. $PbTiO_3$ possess a rhombohedrally distorted perovskite structure**.**

a). ***Multiferroic compounds with Perovskite structure****:* These compounds have either ABO_3 or $A_2B´B´´O_6$ as the general chemical formula. For magnetism one needs partially filled d shells of a transition metal, ferroelectricity in these systems is caused by the off-centre shifts

of the transition metal ion, which forms strong covalent bonds with one (or three) oxygen, using their empty d states [Fig. 1.a]. Example – $BaTiO_3$, $Pb(ZrTi)O_3$.

b). ***Geometric ferroelectricity:*** Ferroelectricity in $YMnO_3$ [8] is caused by the tilting of the practically rigid MnO_5 with a magnetic Mn remaining at the centre and not due to the magnetic Mn^{3+}, but, this tilting occurs just to provide closer packing, and as a result the oxygen ions move closer to the rather small Y ions [Fig. 1.b].

c). ***Multiferroic character due to lone pair:*** This type of multiferroicity is shown in $BiFeO_3$, and probably in $BiMnO_3$, and PVO_3, where Bi^{3+} and Pb^{2+} results in the origin of ferroelectricity. As the two 6s electrons present in these ions do not participate in bond formation hence are called lone pair. This leads to high polarizability-the condition required for ferroelectricity. In $BiFeO_3$, $Pb(Zr_xTi_{1-x})O_3$ compounds the ordering of these lone pairs (with certain admixture of p orbital) in one direction results not only in the origin of ferroelectricity but also improves it [Fig. 1.c].

d). ***Charge ordered Multiferroic:*** This type of multiferrocity is often observed in transition metal compounds, especially those formally containing transition metal ions with different valence. Ferroelectricity in these types of multiferroics appears if both bonds and sites turns out to be in-equivalent after charging [Fig. 1.d]. Example: $Pr_{1/2}Ca_{1/2}MnO_3$ [9] or in rare earth (R) nickelates $RNiO_3$ [10], with charge ordering.

1.3.1.2 Multiferroic of Type-II:

In comparison to type-I these are recently discovered materials in which ferroelectricity is caused by magnetism which infer strong coupling between the two; these are the types of multiferroics in which ferroelectricity is caused by a special or particular type of magnetism [11, 12]. These materials possess much smaller polarization (10^{-2} $\mu C/cm^2$).

Examples:

i). $TbMnO_3$, T_{N1}=41K the magnetic ordering occurs, and at T_{N2}=28K the magnetic structure changes.

ii). $TbMn_2O_5$ also shows this type of behaviour.

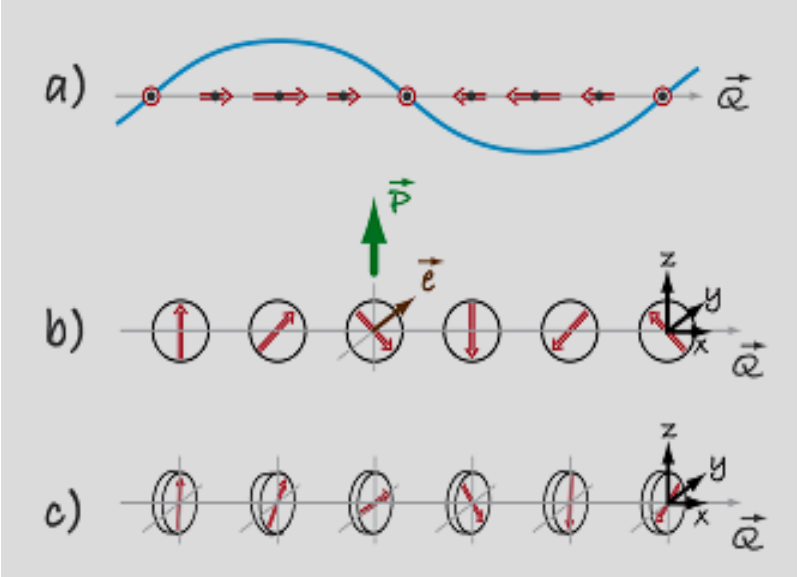

Fig.1.2 The Different type of spin structures relevant for type-II multiferroics. (a) Sinusoidal spin density wave, in which spins point along one direction but vary in magnitude. This structure is centrosymmetic and consequently not ferroelectric. (b) The cycloidal spiral with the wave vector Q = Qx and spins rotating in the (x, z)-plane. It is in this case where one finds nonzero polarization, $P_z \neq 0$. (c) In a so-called "proper screw" the spins rotate in a plane perpendicular to Q. Here the inversion symmetry is broken, but most often it does not produce polarization, although in certain cases it might [13].

Multiferroics of type-II are further divided into following categories:

a). ***Collinear magnetic structures Multiferroics of Type-II:*** These types of multiferroics are those in which ferroelectricity appears in collinear magnetic structures which implies that the alignment of all magnetic moments along particular axis without the compulsion of spin-orbit interaction. These materials can show polarization as a result of exchange striction as the magnetic coupling varies with atomic positions. Example: Ca_3CoMnO_6. [14].

b). ***Multiferroics of Type-II Spiral:*** In these types of multiferroics ferroelectricity appears along with spiralling magnetic phase generally of cycloid type. There are a number of multiferroics of type-II which belong to this subgroup.

Example: $Ni_3V_2O_6$, $TbMnO_3$ and $MnWO_4$, in $TbMnO_3$ though all the spins points in a particular direction but the amount of local moment varies periodically in space below T_N=41K and below T_N=28K the tip of the spins of Mn order in such a way that they form a cycloid [Fig.1.2].

1.4 Applications of Multiferroic Material:

Multiferroic materials are explored for a number of applications either in bulk or thin film.

i). In bulk Composite structures: high-sensitivity a.c. magnetic field sensors and electrically tunable microwave devices such as filters, oscillators and phase shifters.

ii). In multiferroic thin films: magnetoelectronic devices, spintronics devices such as tunnel magnetoresistance (TMR) sensors.

iii). Multiferroic have potential for applications as actuators, switches, magnetic field sensors or new types of electronic memory devices.

Among all the multiferroic materials studied so far, $BiFeO_3$ (BFO) that exhibits the coexistence of ferroelectric and antiferromagnetic (AFM) orders has received great attention due to its high ferroelectric Curie point (T_C~1103 K) and the antiferromagnetic (AFM) Néel point (T_N~647 K). BFO is one of the prime candidates for room-temperature magneto electric applications.

1.5 Bismuth ferrite:

$BiFeO_3$ is an inorganic chemical compound with a perovskite structure. It was first produced in the late 1950s. Bismuth ferrite has always been considered to be antiferromagnetic its bulk form, it is ferroelectric multiferroic having an antiferromagnetic Néel temperature of T_N=643 K and the ferroelectric Curie temperature of T_C=1103 K. One interesting thing should be noted that $BiFeO_3$ possesses the perovskite and not the 'ferrite' structure, despite its nomenclature. Bismuth Ferrite in bulk form can be described as a rhombohedrally distorted ferroelectric perovskite having the space group R3c. The lattice parameters of the rhombohedral unit cell are a = 5.59 Å and $\alpha = 60.68^{\circ}$. In this distorted structure, the R3c symmetry allows the development of spontaneous polarization (Ps) along the pseudo cubic [111] direction. It is observed that each Fe^{+3} spin is surrounded by six antiparallel spins on the nearest Fe neighbours, that is, a G-type antiferromagnet. This implies

that magnetic moments of iron are ferromagnetically coupled within the pseudocubic (111) planes and are anti-ferromagnetically coupled between adjacent planes.

1.5.1 Crystal Structure:

Bismuth Ferrite possesses the phase of rhombohedral (point group R3c) at room-temperature [15]. The lattice parameter of rhombohedral unit cell has, a_{rh}, of 3.965Å and the rhombohedral angle, α_{rh} of calculated 89.3–89.48˚ at room temperature [15], also having ferroelectric polarization along [111] pseudo cubic [15]. The hexagonal frame of reference can also be used to describe the unit cell, with the hexagonal c-axis parallel to the diagonals of the perovskite cube, i.e., [001] hexagonal parallel to [111] pseudo cubic. The lattice parameters of hexagonal unit cell are a_{hex}=5.58Å and c_{hex}=13.90Å [15-17]. The thermal expansion coeffient is neither completely linear nor isotropic [16-18], and the reported values [19, 20] differ notably, ranging from $6.5x10^{-6}$ to $13x10^{-6}$ K^{-1}.

1.5.2 Dielectric properties:

The dielectric constant of $BiFeO_3$ in GHz at room temperature was calculated and found to be ε_r=30 [20, 21, 22, 23]. The value of dielectric constant peaks at the rhombohedral–orthorhombic transition at 825–840˚C, the reason may be due to a ferroelectric–paraelectric transition. The dielectric constant is small as compared to those of typical perovskite ferroelectrics eg. $BaTiO_3$, $(Ba,Sr)TiO_3$ and $Pb(Zr,Ti)O_3$ (PZT). The mean refractive index, n, of Bismuth Ferrite is calculated and and found to be 2.62 [39], therefore optical frequency dielectric constant can be predicted as $\varepsilon_r = n^2 = 6.86$. This, however; is only an average value; Bismuth Ferrite is in fact strongly birefringent with Δn=0.34 [24] which means that the dielectric constant is anisotropic at optical frequencies.

1.5.3 Ferroelectricity:

1.5.3.1 Bulk: In bulk form Bismuth Ferrite is a room-temperature ferroelectric, having spontaneous electric polarization which is directed along one of the [111] directions of the perovskite structure. The spontaneous polarization is 3.5 μC/cm^2 along the [100] direction and 6.1 μC/ cm^2 in the [111] direction at 77 K [25], which is smaller than expected for a material with such a high Curie temperature. Because the ferroelectric state is attributed to a large displacement of the Bi ions relative to the FeO_6 octahedra, this leads to the following important consequence. The ferroelectric polarization of BFO lies along the <111>

direction, leading to the formation of eight possible polarization directions (positive and negative orientations along the four cube diagonals).

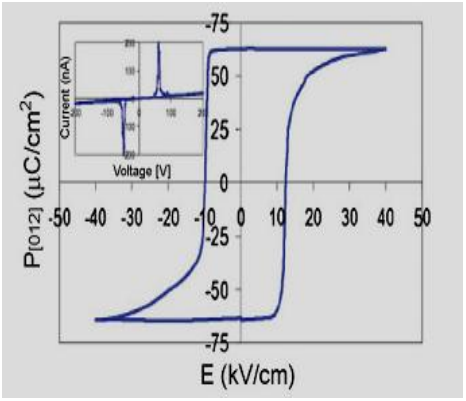

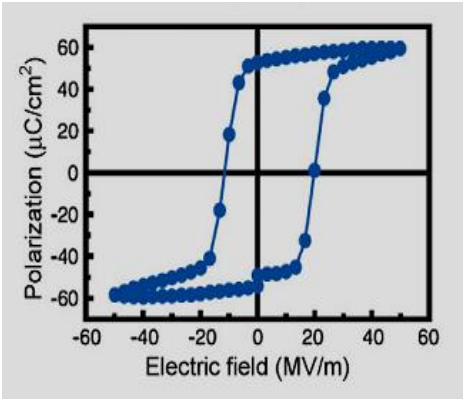

Fig.1.3 Polarization of $BiFeO_3$: bulk single crystal [26]. **Fig.1.4** Polarization of $BiFeO_3$: Epitaxial thin film [27].

1.5.3.2 Thin Films: In addition to having excellent ferroelectric properties, thin films of $BiFeO_3$ often have different crystallographic structures than single crystals do. Free standing dendritic films were prepared as early as the mid 1980s by H. Schmid and others in Geneva, and these are like single crystals. In particular, their crystal class at ambient temperatures is rhombohedral. However, when bismuth ferrite is epitaxially grown as a thin film onto, for example, an $SrTiO_3$ [001] substrate, the resulting morphology is monoclinic, where the symmetry-lowering distortion arises from in-plane contraction and out- of-plane elongation as a result of lattice mismatch between film and substrate. In the case of the $SrTiO_3$ substrate, a room temperature spontaneous polarization of 50–60 $\mu C/cm^2$ was obtained, almost an order of magnitude higher than that of the bulk [28].

1.5.4 Magnetism:

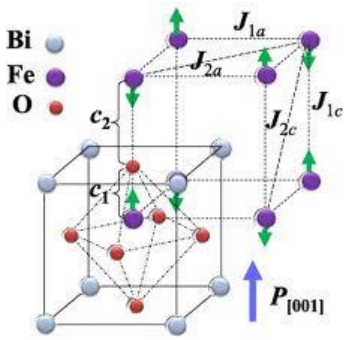

Fig.1.5 The G- type antiferromagnetism of $BiFeO_3$.

The local short-range magnetic ordering of $BiFeO_3$ is G-type anti-ferromagnet, that is, each Fe^{+3} spin is surrounded by six anti-parallel spins on the nearest Fe neighbours. The spins

are in fact not perfectly anti-parallel, as there is a weak canting moment caused by the local magnetoelectric coupling to the polarization. Superimposed on this canting, however, is also a long-range superstructure consisting of an incommensurate spin cycloid of the anti-ferromagnetically ordered sub lattices. The cycloid has a very long repeat distance of ca. 62–64 nm, and a propagation vector along the [110] direction [29, 30]. The magnetic easy plane (the plane within which the spins rotate) is defined by the propagation vector and the polarization vector.

1.5.5 Domains and domain walls:

The behaviour of domains is directly responsible for i) switching characteristics (switching of polarization takes place through nucleation and growth of domains) and ii) domain size scales with sample size, so thin films can have very small domains and, therefore, a high volume density of domain walls. The $BiFeO_3$ displays new domain-wall related phenomena of its own which make this subject particularly fascinating. In rhombohedral $BiFeO_3$ the ferroelectric polarization can point along any of the four diagonals of the perovskite unit cell, with two anti-parallel polarities for each direction: hence there are eight different polar domains in $BiFeO_3$. Separating adjacent domains, there are three possible types of ferroelectric domain wall, which are usually labelled according to the angle formed between the polarization vectors on either side of the wall. When only one component of the diagonal polarization is reversed (say, one domain has [111] orientation and the adjacent one is $[11\bar{1}]$), then the polar vectors form an angle of approximately 71˚ and the domain wall that separates the two polarizations is called a 71˚ wall. When two polar components are reversed, it is a 109˚ wall, and when all three components of the polarization are reversed it is a 180˚ wall.

1.5.6 Bismuth Ferrite Nanotubes, Nanowires, and Nanocrystals:

There is a fast-growing body of research devoted to the manufacture and characterization of complex nanoscopic shapes other than thin films. These 3D nanostructures generally have their own distinctive size effects, and multiferroic $BiFeO_3$ is no exception. For example, nanocrystals of $BiFeO_3$ show enhanced magnetization and superparamagnetism correlated with decreasing diameter [34]. Similar size-induced magnetism has also been reported for $BiFeO_3$ nanowires [35] and nanopowders [36]. This is thought to be due to the large fraction of uncompensated spins from the surfaces of the nanocrystals, an effect that is

well known from classic antiferromagnets such as NiO [37]. Wong reported crystalline $BiFeO_3$ nanotubes in 2004 [38]. These tubes were 240–300 nm in diameter and as much as 50 mm long. Prepared via a sol-gel technique and a porous alumina (AAO) template technique, they were polycrystalline with some amorphous content. Those authors removed the alumina template completely by immersion in NaOH, meaning that the tubes were left out in a pile which was hard to characterize electrically. Zhang *et al*. [39] used porous alumina templates instead, managing to make ordered arrays of standing $BiFeO_3$ nanotubes and measure their piezoelectric hysteresis loops. This proved that they were indeed ferroelectric.

1.5.7 Resistivity of Bismuth Ferrite:

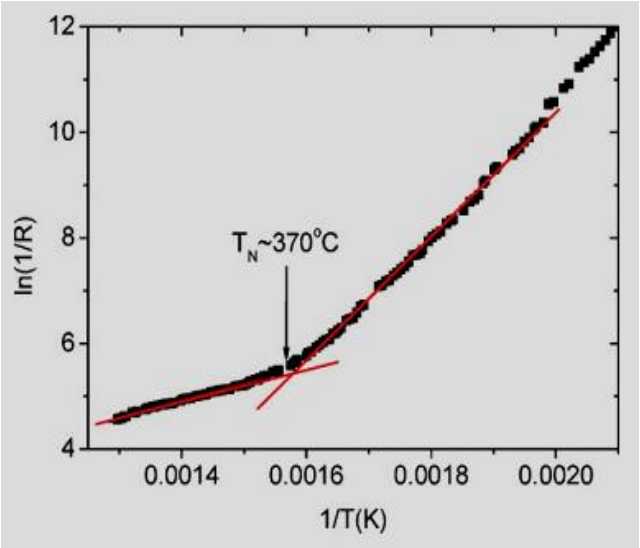

Fig.1.6 Arrhenius plot of the two-probe resistivity of a single crystal, showing a change of slope at the Néel temperature.

The dc resistivity of good-quality bulk samples of $BiFeO_3$ exceeds 10^{10} Ohm cm. [31, 32]. As temperature increases, the resistivity decreases as would be expected from any wide-band gap semiconductor. Around the T_N (370˚C) there is no change in the absolute value of resistivity, but Arrhenius plots show a change in slope, with the activation energy of the charge carriers decreasing from ca. 1.3 to ca. 0.6 eV as the material is heated above T_N. Resistive anomalies at T_N have also been reported by Selbach et al. [33]. At even higher temperatures there are further resistive anomalies correlated with the α-β (rhombohedral–orthorhombic) transition, the β-γ (orthorhombic–cubic) transition and, finally, the decomposition temperature [31]. Specifically, the resistivity decreases (but remains semiconducting) at the α-β transition [33].

1.5.8 Device applications:

Being a room-temperature multiferroic, $BiFeO_3$ is an obvious candidate for applications. The remnant polarization of $BiFeO_3$ is very large, $100\mu C/cm^2$ along the polar [111] direction. To put this into context, this is the biggest switchable polarization of any perovskite ferroelectric, and is roughly twice as big as the polarization of the most widely used material in ferroelectric memories, PZT. Moreover, unlike PZT, $BiFeO_3$ is a lead-free material, a bonus regarding health and safety. It is therefore not surprising that manufacturers of ferroelectric memories such as Fujitsu are considering $BiFeO_3$ as the potential active material in their next generation of ferroelectric memory devices.

1.5.9 Bismuth ferrite at room temp:

It is both antiferromagnetic—its magnetic moments align in opposing directions, so that the net magnetization is zero—and ferroelectric, bismuth ferrite is multiferroic in the popular use of the term. Since it is readily synthesized in bulk and thin-film forms and both its antiferromagnetic Néel temperature and ferroelectric Curie temperature are well above room temperature (approximately 643 K and 1103 K, respectively). Leakage currents in ferroelectrics are usually considered a serious problem. However, there may be an advantage for diode-like applications, since the direction of the ferroelectric polarization can influence the magnitude of electrical conduction. Single, $BiFeO_3$ crystals exhibit significant conduction due to their small optical band gap and, possibly, to the presence of oxygen vacancies, and consist of a single ferroelectric domain without grain or domain boundaries. The result is a strong correlation between polarization direction and electronic conduction, which can produce diode-like unidirectional current flow.

LITERATURE REVIEW:

While a considerable effort of many research groups aims at designing and synthesizing new materials that would be ferroelectric and would possess a net magnetization at the same time, the main obstacle in the applications of these materials remains their low magnetic ordering temperature. The most- studied room-temperature multiferroic, $BiFeO_3$, is an antiferromagnet, i.e. its net magnetization is zero. Ferromagnetic oxides in general are scarce, even without imposing the additional request of ferroelectricity. $BiFeO_3$ is the most interesting in the family of very few single-phase multiferroics because of its high phase transition temperatures (i.e., Curie temperature ∼1083 K, and Néel temperature ∼657 K) [40]. Since its discovery in the 1960s, difficult synthesis of $BiFeO_3$ and its large current leakage have hampered its practical applications.

Doping of various elements like La^{+3}, Ba^{+2}, Ca^{+2}, Cr^{+3} etc. enhances various properties like magnetic properties, ferro-electrical properties, dielectric properties, magnetoelectric properties etc. In ABO_3 type multiferroic with ferroelectric nature due to lone pair of electron A site doping influences the ferroelectric nature and B site doping has an effect on magnetic character. A number of dopants are used to enhance the desired properties via doping of different elements some of them are listed below.

A site dopants – Sr^{+2}[41], Sm^{+3}[42], La^{+3}[43], Ba^{+2}[44], Ca^{+2}[44], K^{+}[48], Y^{+3}[49]

B site dopants **-** Nb^{+5}[41], Ti^{+4}[42], Nb^{+5}[43], Ni^{+3}[45], Mg^{+2}[46], Cr^{+3}[47], Mn^{+3}[47]

C. Lang *et al.* [50] synthesized $Bi_{0.9}La_{0.1}FeO_3$ (BLF) and $Bi_{0.9}La_{0.1}Fe0._{98}Zr_{0.02}O_3$ (BLFZ) ceramics by conventional solid state reaction method. X-ray diffraction studies show that both posses same rhombohedrally distorted perovskite structure with space group R3c. The magnetic properties of BLF and BLFZ ceramics were grains of BLFZ were greatly reduced and became homogeneous in comparison with BLF. BLFZ showed much enhanced

remnant magnetization, which was attributed to the collapse of the spiral spin structure. Exchange bias and large coercivity were observed in BLFZ. The Néel temperature of BLFZ remains the same with BLF (~355˚C).

M. Kumar *et al.* [51] synthesized single-phase multiferroic $BiFeO_3$ ceramics using sol– gel technnique. However, the annealing under Ar atmosphere was effective in reducing impurity phases but created large oxygen vacancies and the composition was $BiFeO_{2.75}$ rather than $BiFeO_3$. The oxygen vacancies associated with Fe^{+2} were responsible for ferromagnetic ordering in Ar annealed BFO ceramic. In addition, both the ceramics showed weak ferroelectric characteristics at room temperature.

M. Yasin Shami *et al.* [52] synthesized BFO nanopowders for different pH values (8–13) by a simple co-precipitation method. The as synthesized powders were amorphous in nature. The phase purity of the BFO samples was confirmed from XRD analysis. The crystallite size was in the range of 48–62 nm for all the samples, and the maximum value was observed for pH= 10. The SEM images revealed a granular microstructure with a wide range of size distribution. The maximum value of the dielectric constant (600) was observed for the sample with pH = 10. The central frequencies of the relaxation peaks have a varying trend for different pH values.

Z. X. Cheng *et al.* [53] synthesized $Bi_{1-x}La_xFeO_3$ ceramics with x = 0, 0.1, 0.2, and 0.3 by solid state reaction, starting from metal oxide. They reported that below 10% La doping, $Bi_{1-x}La_xFeO_3$ maintains the rhombohedral structure of $BiFeO_3$. However, for $Bi_{0.8}La_{0.2}FeO_3$ and $Bi_{0.7}La_{0.3}FeO_3$, the structures change to the orthorhombic and tetragonal, respectively. La doping significantly reduces electric leakage and leads to successful observation of electrical polarization hysteresis loops. Doping with La also enhances the ferromagnetic moment, due to the broken cycloid spin structure caused by the changes in the crystalline structure.

R. Das *et al.* [54] prepared $Bi_{1-x}La_xFeO_3$ (x =0.0 and x=0.25) ceramics by chemical synthesis route and found that magnetic and ferroelectric properties of BFO change significantly with Ba substitution in place of Bi. Above the Néel temperature of pure BFO, a large enhancement in magnetization was observed in Ba doped samples. Transition temperatures (magnetic and ferroelectric) shift towards higher temperature with the increase in dopant concentration.

S. Mukherjee *et al.* [55] doped bismuth ferrite samples with pure and rare Earth transition metal (7.5% and 10% lanthanum, yttrium) and synthesized the samples through chemical solution route. Crystallization temperature around 450˚C was observed from thermal analysis by DTA-TGA and subsequent XRD analysis of the annealed samples showed that the crystallites were mainly rhombohedral with R3c space group with an expected impurity phase. Morphological analysis using FESEM and AFM revealed the samples to be of agglomerated nature and optical analysis by UV-VIS spectroscopy showed a decrease and increase in the band gap due to La and Y doping respectively.

Summary of Literature Review:

- Variety of techniques is used to synthesis $BiFeO_3$.
- The most simple and cost effective method of synthesis of $BiFeO_3$ is autocombustion route where reaction time is less.
- Doping of different elements in BFO leads to change in the structural, optical, magnetic, ferroelectric and electrical properties of BFO.

Objective of the Present Study:

The main objective is to produce $BiFeO_3$ which must have the following characteristics:

1. To synthesize and characterise pure phase $BiFeO_3$ material.

2. To investigate the effect of La doping on structural, optical and dielectric properties of BFO sample.

CHAPTER - 3

SYNTHESIS AND CHARACTERIZATION TECHNIQUES:

3.1 SYNTHESIS:

The various methods which are generally used for the synthesis of $BiFeO_3$ are:

• Co-precipitation Method

• Solid state reaction Method

• Auto-combustion Method

3.1.1 AUTO-COMBUSTION METHOD:

The most widely used and useful method of preparation of BFO is the combustion synthesis route using a fuel. Combustion synthesis is becoming one of the most popular methods for the preparation of a wide variety of materials. This method is rapidly emerging as one of the most-convenient methods for the preparation of oxide materials. The main advantage of using this technique is due to the simplicity, the broad applicability range, a low temperature synthesis technique that offers a unique mechanism via a highly exothermic redox reaction to produce oxides., the possibility of obtaining products in the desired size and shape. The fuel used may be glycine ,citric acid or urea .The precursor material used for the synthesis of BFO by auto-combustion route are $BiNO_3$ and $FeNO_3$ solutions with a certain concentration level. An aqueous solution of a redox system constituted by the nitrate ions of the metal precursor, acting as oxidizer, and a fuel like urea, glycine, citric acid or many others is heated up to moderate temperatures and, upon dehydration, the strongly exothermic redox reaction develops, which is generally self-sustaining and provides the energy for the formation of the oxide.

The process is based on the mixing of reactants that oxidize easily, such as metal nitrates, and an organic fuel, acting as a reducing agent. An external heat supply is needed to initiate the ignition of the mixture leading to a self-sustainment of an exothermic redox reaction. In this technique, based on the principles of the propellant chemistry, a thermally induced redox reaction takes place between an oxidant and a fuel. Many types of combustion

synthesis exist which differ mainly in the physical state of the reactants or in the combustion modality. By combustion-based methods it is possible to produce monophasic nanopowders with homogeneous microstructure, at lower temperatures or shorter reaction times, if compared with other conventional methods like solid-state synthesis or nitrate method.

The various advantages of adopting combustion synthesis as the prime method for the production of BFO are as follows:-

- Self-purifying feature due to the high temperatures involved.
- The possibility of obtaining products in the desired size and shape.
- Simple and cost effective.
- Homogeneous, very fine crystalline nanopowders without the intermediate decomposition and calcination steps which other conventional synthesis routes would require.
- Monophasic nanopowders at lower temperatures or shorter reaction times.

3.1.2 EXPERIMENTAL WORK:

In the present work, La-doped $BiFeO_3$ nanoparticles were prepared by sol gel auto-combustion method. Glycine was used as the fuel because of its high negative combustion heat (-3.24kcalg^{-1}) as compared to urea (-2.98 kcalg^{-1}) and citric acid (-2.76 kcalg^{-1}) [40]. Three samples were prepared with different molar concentration of dopant as given below:-

1. Undoped $BiFeO_3$.

2. 10% La-doped $BiFeO_3$ (BLFO; x=0.1)

3. 20% La-doped $BiFeO_3$ (BLFO; x=0.2)

For undoped $BiFeO_3$, as the starting material bismuth nitrate, iron nitrate, and, glycine were used.

- Solution of $Bi(NO_3)$ was prepared by adding desired amount of HNO_3, as $Bi(NO_3)$ is insoluble in water and $Fe(NO_3)$ was directly added to water.
- Now both the solutions were mixed in the beaker and appropriate amount of glycine was added and stirred until clear solution was obtained.
- The clear solution was then heated on the hot magnetic stirrer and stirred until a dark and viscous solution was obtained.

- The temperature was kept constant and the solution was heated continuously which led to auto ignition along with evolution of large amount of darkish brown fumes.
- The process led to brown coloured powder which was again heated for 2 to 3 minutes to ensure there was no more solution left to be combusted.
- The powder was then collected and calcined at 500˚C for 4 hours.
- The calcined powder was then characterized for crystal structure.

Similar procedure was followed for La-doped $BiFeO_3$, with addition of appropriate amount of $La(NO_3)_3$.

3.2 CHARACTERIZATION TECHNIQUES:

3.2.1 X-Ray Diffraction (XRD):

X-ray powder diffraction (XRD) is a versatile, non-destructive technique that reveals detailed information about the chemical composition and crystallographic structure of natural and synthesized materials. It can also provide the dimensional information on unit cell. The analyzed material is finely ground, homogenized, and average bulk composition which is determined. The XRD is an efficient analytical technique used to identify and characterize unknown crystalline materials. Monochromatic X-rays are used to determine the inter-planar spacing of the unknown materials. Samples are analyzed as powders with grains in random orientations to ensure that all crystallographic directions are "sampled" by the beam. When the Bragg conditions for constructive interference are obtained, a "reflection" is produced, and the relative peak height is generally proportional to the number of grains in a preferred orientation.

Bragg's law:

Fig.3.1 shows, when a crystal is bombarded with X-rays of a fixed wavelength and at certain incident angles, intense reflected X-rays are produced when the wavelengths of the scattered X-rays interfere constructively. In order for the waves to interfere constructively, the differences in the travel path must be equal to integral multiples of the wavelength.

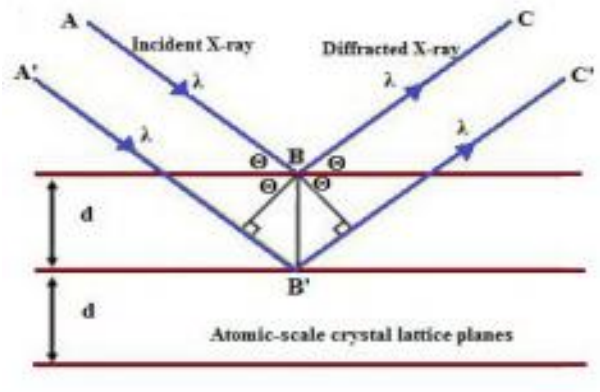

Fig.3.1 Schematic for Bragg's Law.

When this constructive interference occurs, a diffracted beam of X-rays will leave the crystal at an angle equal to that of the incident beam. To illustrate this feature, consider a crystal with crystal lattice planar distances "d". Where the travel path length difference between the ray paths of two beams (ABC and A'B'C') is an integral multiple of the wavelength, constructive interference will occur for a combination of that specific wavelength, crystal lattice planar spacing and angle of incidence (θ). Each rational plane of atoms in a crystal will undergo refraction at a single, unique angle (for X-rays of a fixed wavelength). According to Bragg's Law:

i.e.

$$2\,d\,\mathrm{Sin}\,\theta = n\lambda \qquad \text{... (i).}$$

where n is an integer that indicates the order of reflection, λ is the wavelength of the incident X- rays, d is the inter-planar spacing of the crystal and θ is the angle of incidence.

3.2.2 LCR meter:

In LCR meter ("L" represents Inductance, "C" represents Capacitance and "R" represents Resistance) is a piece of electronic test equipment which is used to measure the inductance, capacitance and resistance of a component. These quantities are not directly measured in the usual version of the instrument but these determined from the measurement of impedance. The necessary calculations are, however, incorporated in the instrument's circuitry; the meter reads L, C and R directly with no human calculation required.

Fig. 3.2 Represents the HIOKI 3532-50 LCR meter.

Fig.3.2 represents the HIOKI 3532-50 LCR meter used for dielectric measurements which is the most flexible RCL meter and allows testing with any frequency up to 1 MHz. The AC and DC test voltages are continuously adjustable and the instrument offers a built-in contact check to ensure optimum connection. With these capabilities, you can handle a wider variety of components and under more realistic test conditions.

3.2.3 UV Spectroscopy:

Many molecules absorb ultraviolet or visible light. The absorbance of a solution increases as attenuation of the beam increases. Absorbance is directly proportional to the path length, b, and the concentration, c, of the absorbing species.

Beer Lambert law states that

$$A = \log_{10}\frac{I_o}{I} = e*b*c \qquad \text{... (ii).}$$

where “e” is a constant of proportionality, called the absorbtivity.

Different molecules absorb radiation of different wavelengths. An absorption spectrum will show a number of absorption bands corresponding to structural groups within the molecule. For example, the absorption that is observed in the UV region for the carbonyl group in acetone is of the same wavelength as the absorption from the carbonyl group in diethyl Ketone.

3.2.3.1 Principle of UV Spectroscopy:

Absorption of visible and ultraviolet light produces changes in the electronic states of molecules associated with the electronic states of molecules associated with the excitation of

an electron from a lower to a higher energy level. But it must be noted that each electronic level in a molecule is associated with a number of vibrational sub levels (with small energy separations) and each vibrational level in turn associated with a number of rotational sub levels (with still smaller energy separation). Therefore in its transition to higher energy level, an electron can go from any of the sub levels- corresponding to various vibrational and rotational states-in the ground state to any of the sub-levels in the excited state.

3.2.3.2 The Origin of the Absorptions:

Visible light lies in the wavelength range 4.0–7.0x10^{-7}m.To keep the numbers more manageable, it is usually quoted in nano-metres (10^{-9}m) so that the range becomes 400–700 nm. When light is absorbed by a material, valence (outer) electrons are promoted from their normal (ground) states to higher energy (excited) states.

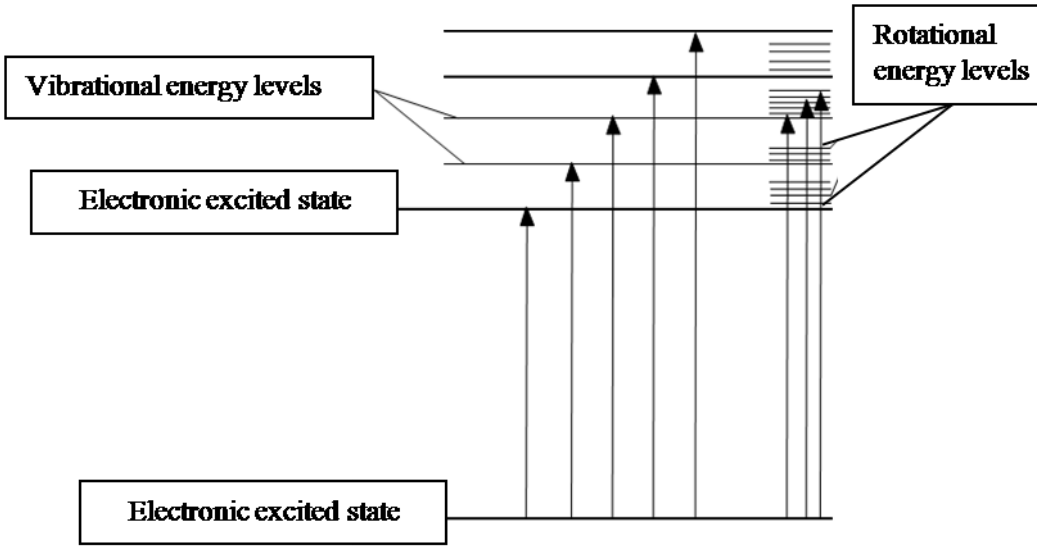

Fig.3.3 Electronic and vibrational levels.

Valence electrons can generally be found in one of three types of electron orbital:

1). single, or σ, bonding orbitals;

2). double or triple bonds (π bonding orbitals); and

3). non-bonding orbitals (lone pair electrons).

Sigma bonding orbitals tend to be lower in energy than π-bonding orbitals, which in turn are lower in energy than non-bonding orbitals.

3.2.3.3 Uses:

In organic molecules and polymers, the U-V visible spectrum can help to identify chromophores and the extent of electronic delocalization. For inorganic complexes the u-v visible spectrum can provide imformation about oxidation states, electronic structures and metal ligand interactions. For solid materials, the u-v visible spectrum can measure the band gap and identify any localized excitation or impurities.

RESULTS AND DISCUSSION:

4.1 XRD Analysis:

The Phase purity, crystal structure and crystallinity of $BiFeO_3$ powder can be estimated using diffraction diffractogram. Fig. 4.1. shows the XRD pattern of the synthesized uncalcined $BiFeO_3$ powder. No characteristic peak is evident in the figure which indicates the amorphous nature of $BiFeO_3$ powder. A thermal treatment is necessary to improve the crystallinity of $BiFeO_3$ ceramics.

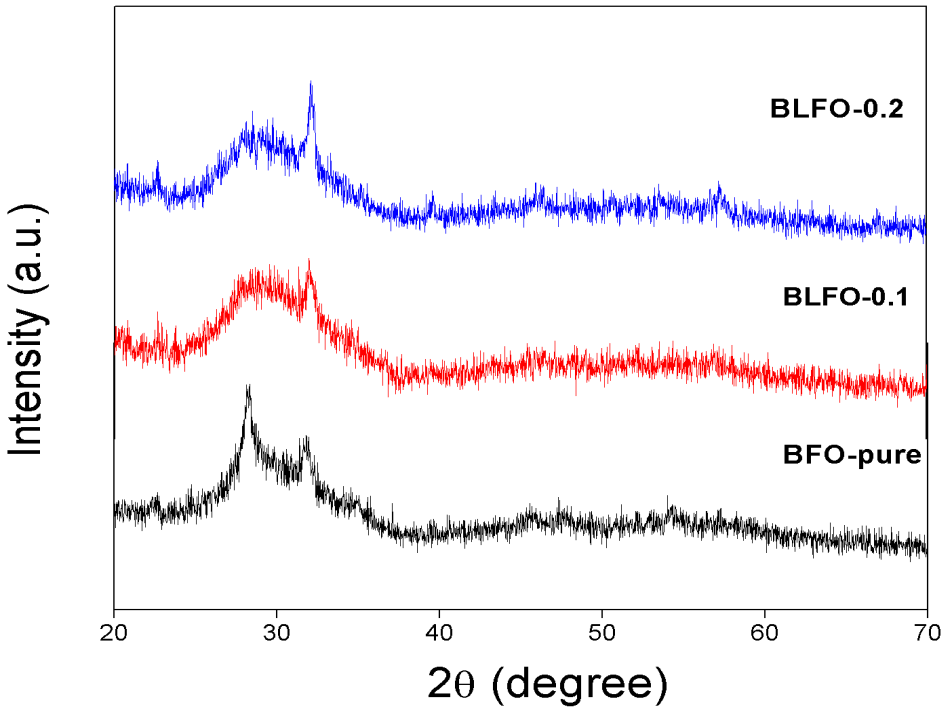

Fig. 4.1 XRD patterns of uncalcined as synthesized undoped and La-doped BFO (x=0.0, 0.1, and 0.2) samples.

Fig. 4.2. shows the X-ray diffraction (XRD) patterns of Pure and La-doped BFO (x=0.0, 0.1, and 0.2) nano-particles calcined at 500˚C. It can be clearly seen that synthesized nano-particles possess high crystallinity since intense peaks have been observed. Pure $BiFeO_3$ nano-particles possess rhombohedral R3*c* structure (JCPDS file no. 71-2494). However, an

extra peak was observed in pure BFO sample, this is identified as the impurity phase, $Bi_{25}FeO_{40}$. which is usually obtained as a minor product due to kinetics of formation.

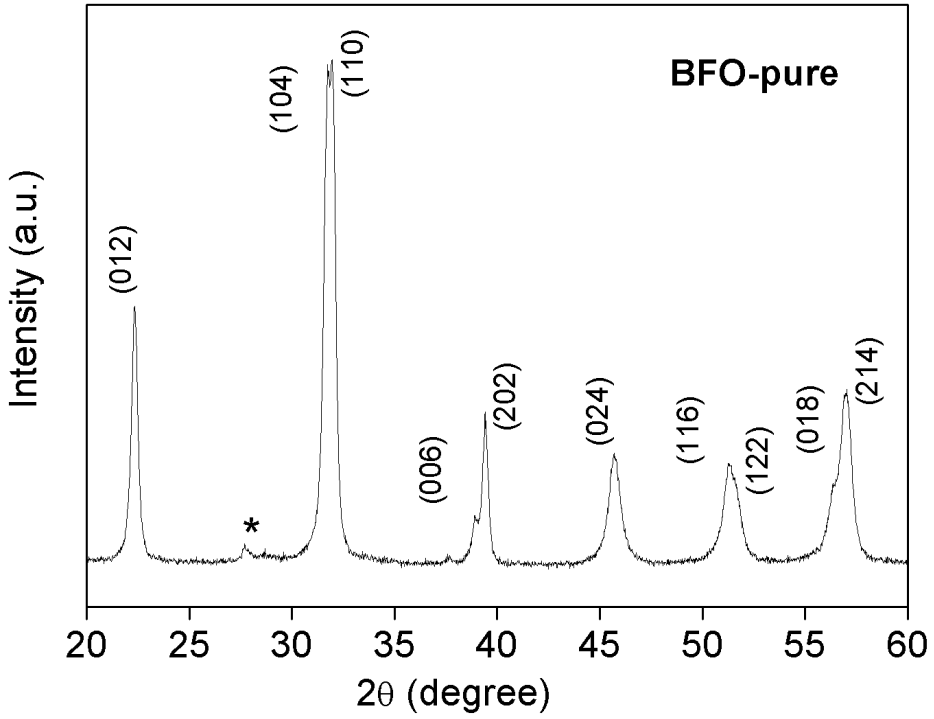

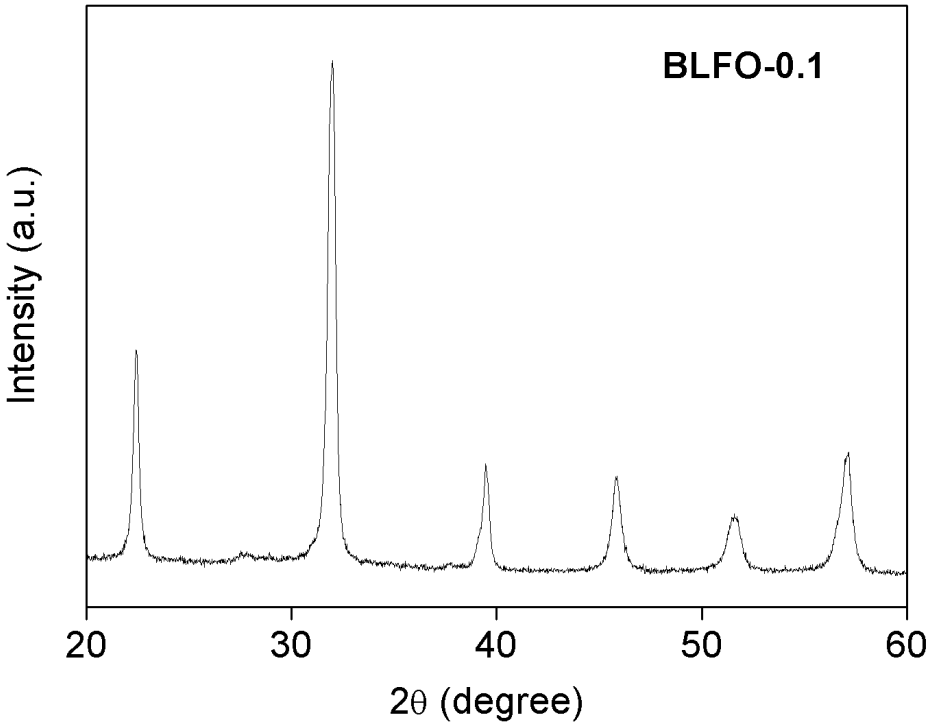

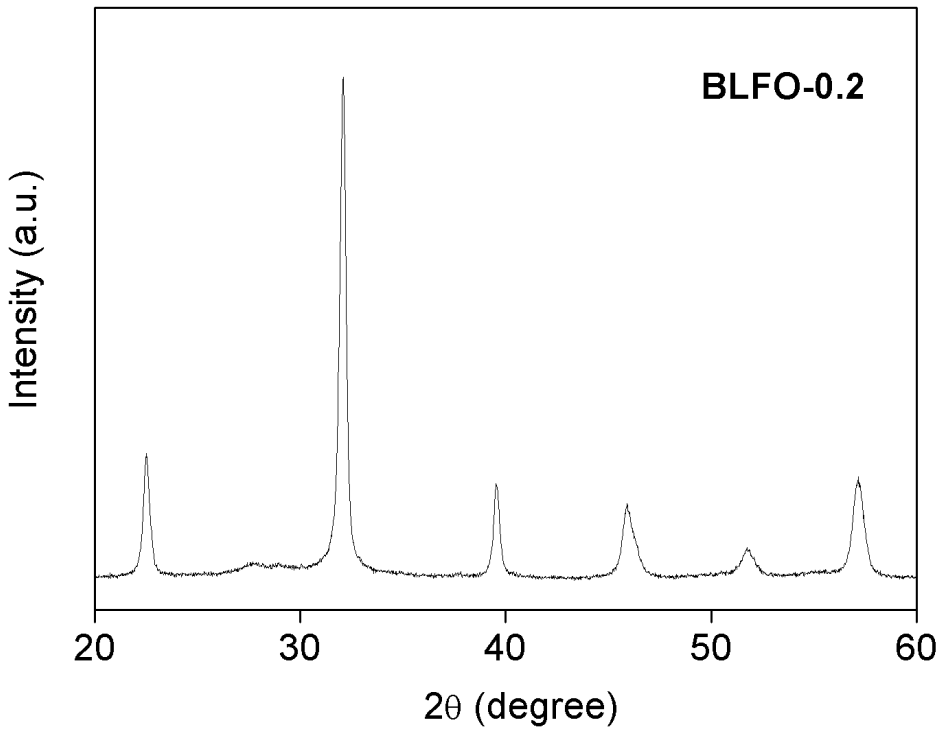

Fig. 4.2 XRD patterns of La doped $BiFeO_3$ ceramics with composition; x=0.0, 0.1, and 0.2 ("*" impurity peak of $Bi_{25}FeO_{40}$ observed in the diffraction pattern recorded at 500°C in pure BFO).

It should be noted that the diffraction intensity obtained from the impurity in the La-doped BFO sample with x=0.1 is weaker than in the pure one, while negligible amount of impurity peaks are observed in x=0.2. This means that doping with La hinders the formation of a second phase.

The substitution of La^{3+} with R_{La}^{3+} = 1.16 Å ions (slightly smaller in size as compared to Bi^{3+}; R_{Bi}^{3+} = 1.17 Å) in $BiFeO_3$ host leads to shifting of characteristic diffraction peaks of doped samples towards right (larger θ) as shown in Fig. 4.3. This indicates a decrease in lattice size and unit cell volume.

The XRD pattern from $BiFeO_3$ particles exhibit broadened peaks which is due to finite size effect and can be described in terms of Scherrer formula. The average crystallite size has been calculated from FWHM of the most prominent diffraction peak using Debye Scherrer equation-

$$d=0.91\lambda/\beta\cos 2\theta \quad \text{... (i).}$$

here,

λ -wavelength of Cu-Kα

β -fullwidth at half maxima

θ -Bragg angle

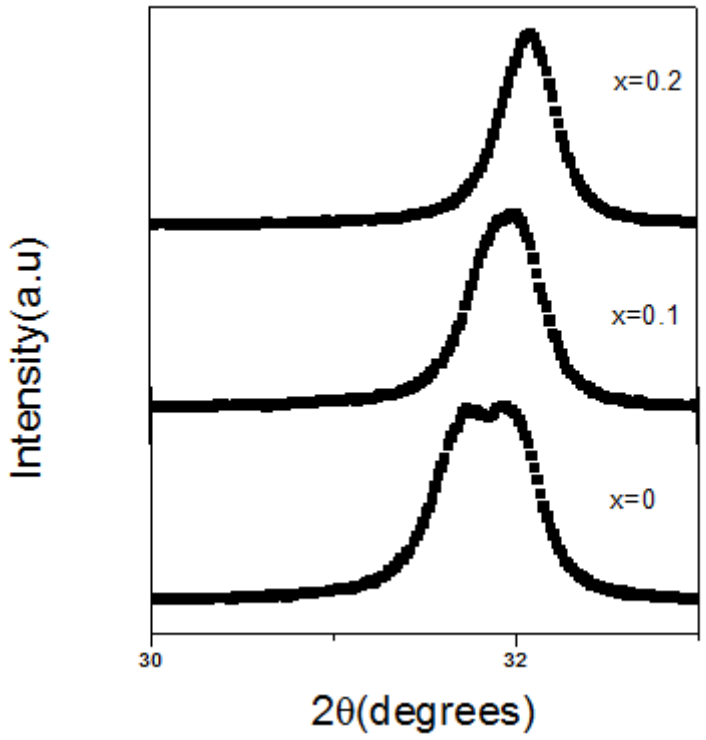

Fig.4.3 Doping dependent evolution of the XRD pattern from 30^{o} to 33^{o}.

Table. 4.1. shows the particle size at different La doping in BFO. From table, it is concluded that with the increase in dopant concentration in sample, the particle size is found to be decreased.

Table 4.1. Particle size at different La doping in BFO.

Sample	**Average crystalline size (nm)**
Pure BFO	d=25.329
0.1% La Doped BFO	d=24.206
0.2% La Doped BFO	d=20.906

The observed decrease in particle-size can be attributed to:-

(i) Doping of La in $BiFeO_3$ inhibiting the crystal growth of nanoparticles and,

(ii) The size of dopant La^{3+} ions being smaller than those of Bi^{3+} ions resulting in the lattice contraction.

In comparison with the pure sample which retains the structure of $BiFeO_3$, the sample with x= 0.1 and 0.2 shows a change from R3C to orthorhombic symmetry, as evidenced by the merging, in the x = 0.1 and 0.2 sample pattern, into one peak of the split diffraction peaks indexed as (104), (110) and (006), (202) around 2θ = 32º and 2θ = 39º in the pattern of x = 0 sample. Similar result is reported by G.S Lotey *et al.* in 2013 [56].

The calculated lattice parameters for rhombohedral (R3*c*) phase have been found to be "a = 5.5876Å", "c = 13.867Å" (hexagonal equivalent). With progressive La doping, there is a significant structure distortion. The structural stability of the perovskite compounds can be quantified by tolerance factor (t) which is defined as:

Tolerance factor describes the stability of the perovskite structure (ABO_3 type) geometrically and is given by

$$t = \frac{r_A + r_B}{\sqrt{2}(r_B + r_O)} \quad \text{... (ii).}$$

where r_A is the average ionic radii of the Bi^{3+} and La^{3+} ions, r_O is the ionic radius of the O^{2-} ion, and r_B is the average ionic radius of the Fe^{3+} and Fe^{4+} ions. Tolerance factor for pure BFO to BLFO (x=0.2) is found to be decreases from 0.8336, 0.8332, and 0.8329 respectively, which indicate that the La doping introduces distortions in sample.

4.2. Optical analysis:

For the photocatalytic activity, it is important to study the optical absorption of the BFO nanoparticles because the UV-vis absorption edge is relevant to the energy band of semiconductor catalyst.

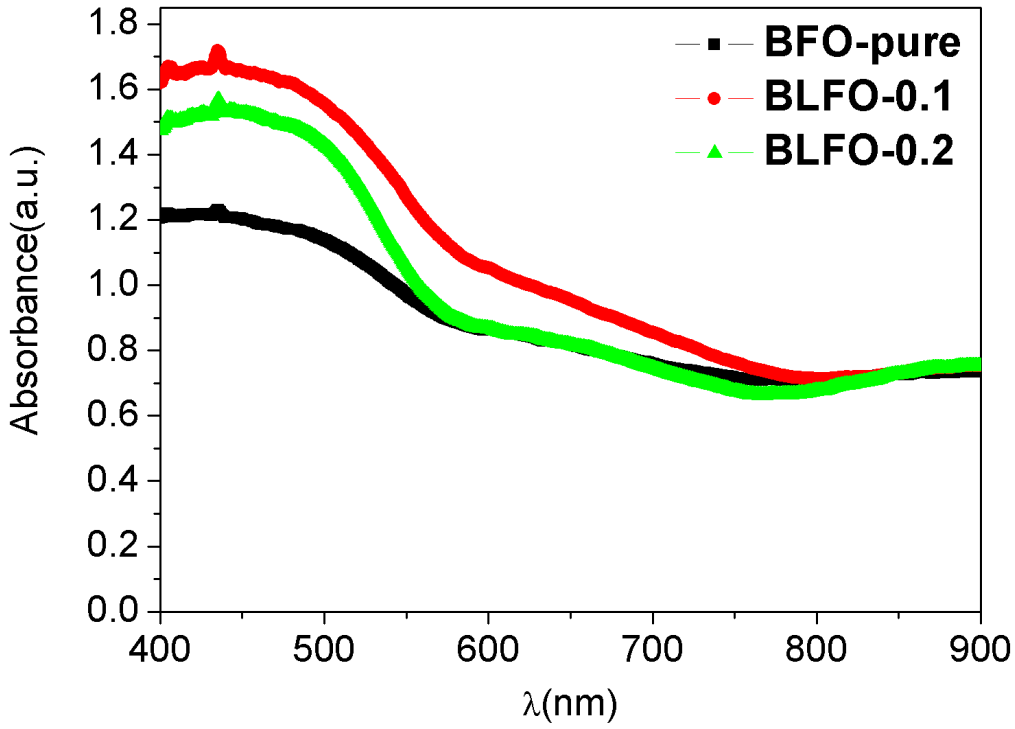

Fig. 4.4 UV-Vis absorption spectra of La-doped BFO (x=0.0, 0.1 and 0.2) samples.

The optical absorption spectra have been recorded using UV-Vis spectrophotometer at room temperature over the range of 400-900nm. Figure 4.4 shows the UV-Vis absorption spectra of different samples. The UV–Vis absorption cut-off wavelength for pure BFO to BLFO (x=0.2) are seen at 814.910, 749.178, and 677.720 nm, respectively. These indicate a change in the electronic structure of $BiFeO_3$ with increase in the dopant concentration. However, as we move to higher dopant concentration, a significant shift of 137 nm towards the shorter wavelength side is observed, which might be due to the creation of oxygen vacancy (Roy *et al.* in 2007) [56]. These indicate an obvious blue shift when $BiFeO_3$ is doped with La and thus an increased bandgap.

The band gap for prepared samples has been calculated from the point of maximum change in slope of $(\alpha h\nu)^2$ with hν. The band gap of La-doped BFO (x=0.0, 0.1, and 0.2) increases from 1.9080 to 2.0805 eV with increase in La doping shown in fig. 4.5. The increase in band gap results in an enhancement of photo catalytic activity in La-doped BFO nanoparticles. The correlation between band gap and photo catalytic activity was also reported by Datta *et al.* in 2008 [58].

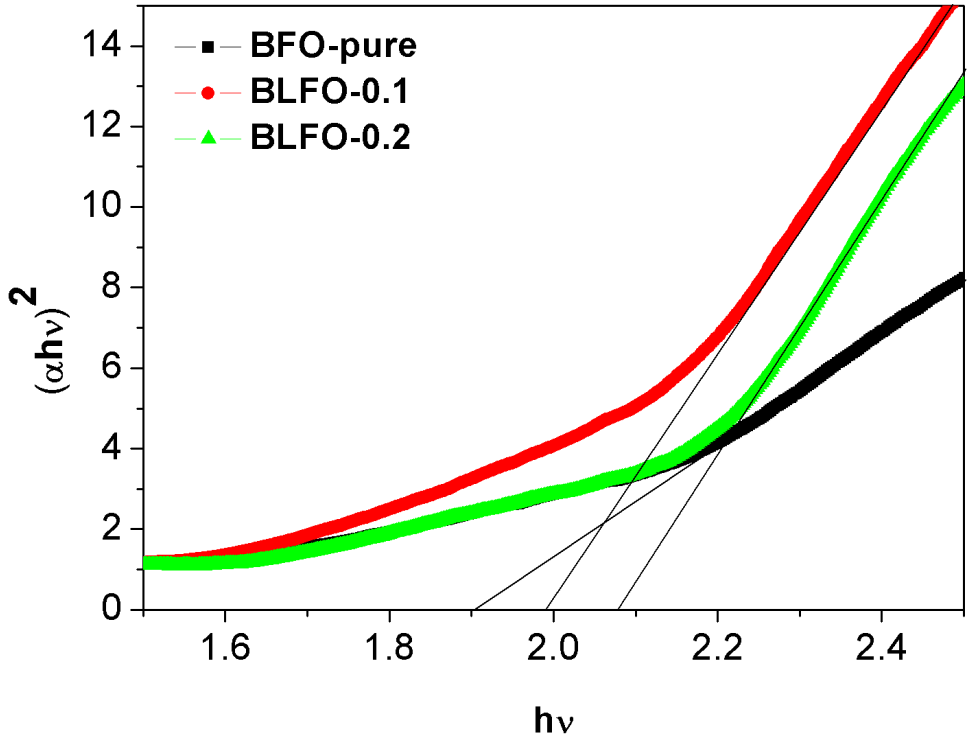

Fig. 4.5 $(\alpha h\nu)^2$ v/s hν graph of pure and doped BFO.

Table 4.2 Energy corresponding to absorption wavelength.

Sample	Absorbance wavelength(nm)	hν (eV)
BFO	814.910	1.9080
10% La-BFO	749.178	1.9980
20% La-BFO	677.720	2.0805

4.3 Dielectric properties:

Dielectric properties of a material indicate the suitability of the material for various electronic applications. The variation of dielectric constant ($\mathcal{E}$) and dielectric loss (tanδ) with frequency of $BiFeO_3$ is shown in Fig. 4.6.

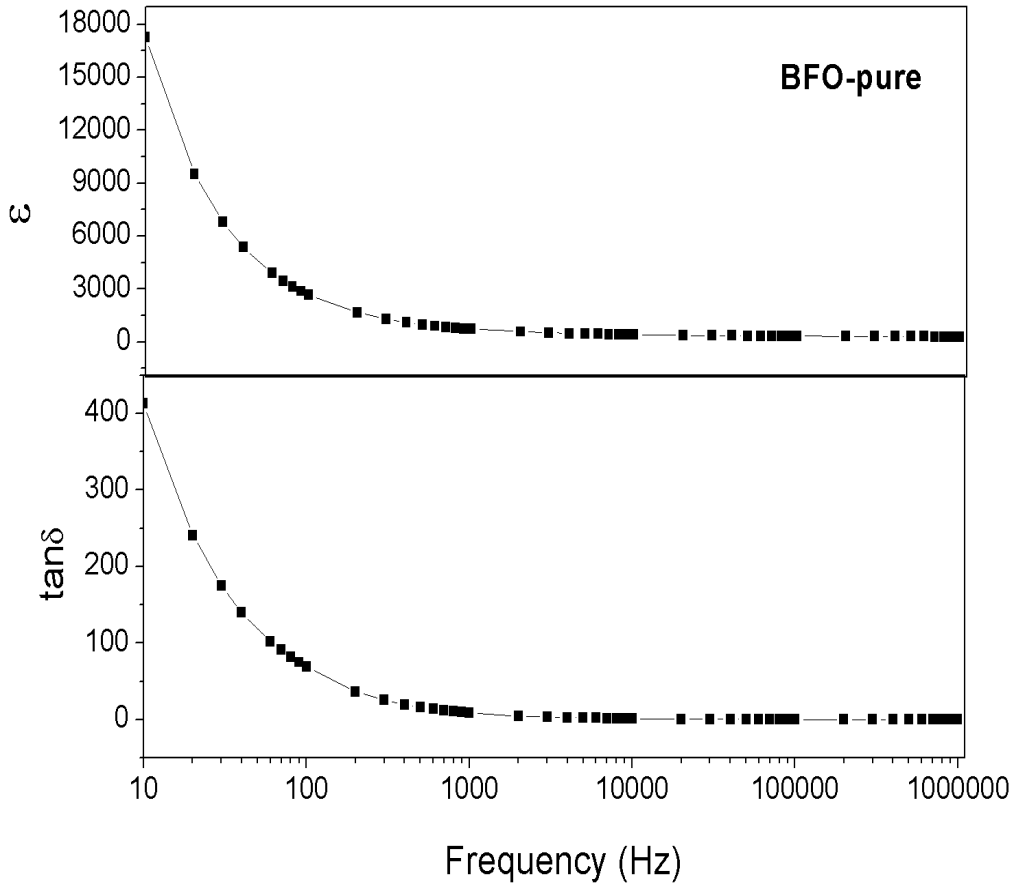

Fig.4.6 Variation of dielectric constant and dielectric loss with frequency for BFO sample.

In the audible range of frequencies, all the polarization (electronic, ionic, orientation and space charge polarizations) are present, but the space charge polarization is prominent as per the theory of dielectric polarization. Space charge contribution depends upon the purity and perfection of the crystals and exhibits itself prominently at low frequencies and is purely surface effect phenomenon. Increase in space charge phenomenon of solid increases the value of $\mathcal{E}$ and tanδ. Extremely high values of $\mathcal{E}$ and tanδ at low frequencies for BFO sample, is an indication of space charge polarization. Both $\mathcal{E}$ and tanδ parameters decrease with increase in frequency upto 1 kHz and as the frequency is increased beyond 1 kHz, both $\mathcal{E}$ and tanδ become almost constant. This can be explained by the phenomenon of dipole relaxation wherein at low frequencies the defects related dipoles are able to follow the frequency of applied field providing high values of $\mathcal{E}$ but begin to lag behind the field with increasing frequency.

Fig. 4.7 shows the effect of La doping on the room temperature dielectric properties. The dielectric loss is reduced with increase in La content. The values of dielectric constant at 1 MHz are 327.6 for BFO, 307.2 for BLFO x=0.1 and 550.2 for BLFO x=0.2. The corresponding tanδ values are 0.27 for BFO, 0.0728 for BLFO x=0.1 and 0.168 for BLFO x=0.2.

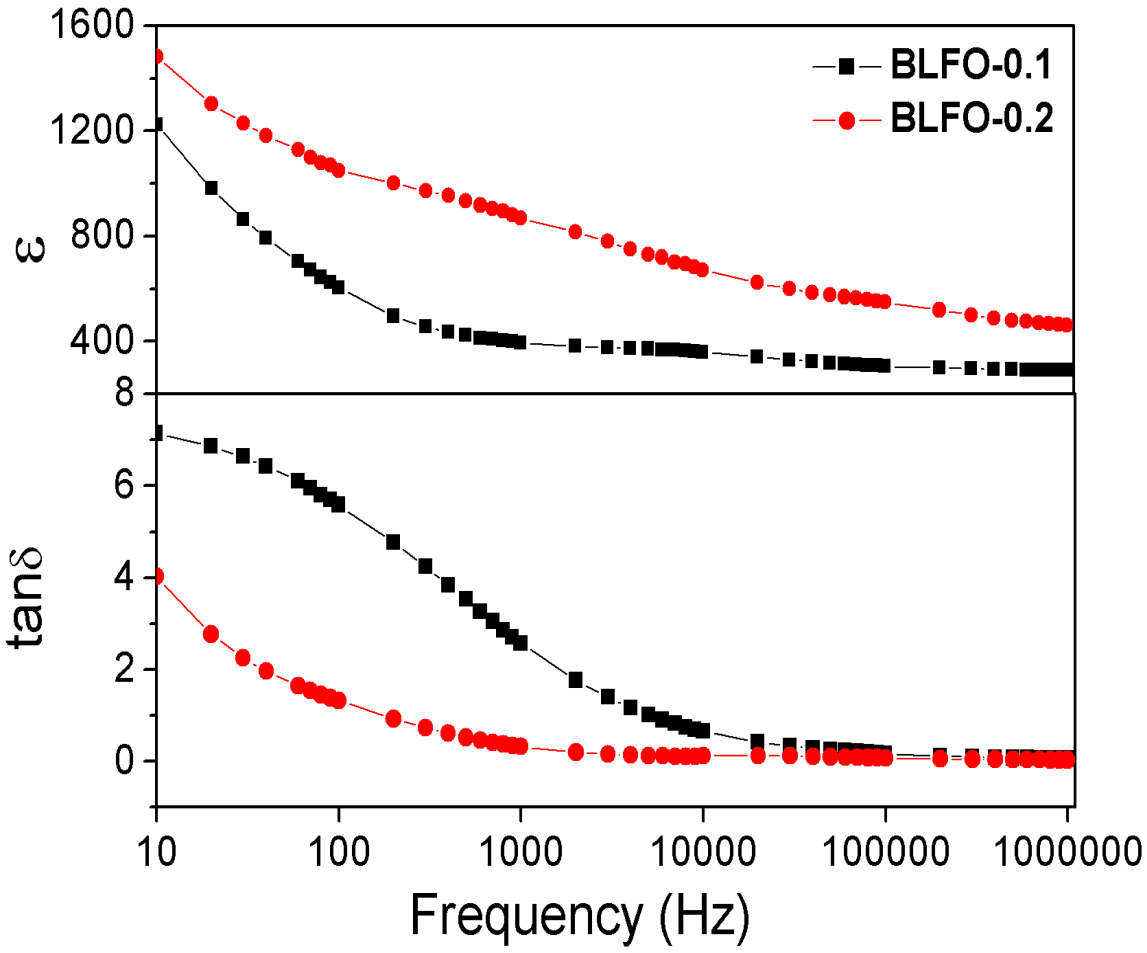

Fig. 4.7 Variation of dielectric constant and dielectric loss with frequency for BLFO x=0.1 and BLFO x=0.2 ceramics.

Fig. 4.8 shows the temperature dependence of dielectric constant (ε) and dielectric loss ($tan\delta$) at 10kHz of BFO and BLFO (x=0.1). The dielectric constant was found to increase with increase in temperature upto 380^{o}C for pure BFO sample and then the dielectric constant decreases with further increase in temperature. This peak corresponds to antiferromagnetic Neél temperature T_N. Similar behavoir was observed for dielectric loss. The effect of La doping is also evident from the figure which indicates a decrease in T_N value

from 380 to 365˚C. Simultaneously the ε_{max} (corresponding to T_N) is increased from 1040.28 for BFO to 1182.12 for BLFO (x=0.1). Observation of T_N is a signature of magnetoelectric coupling.

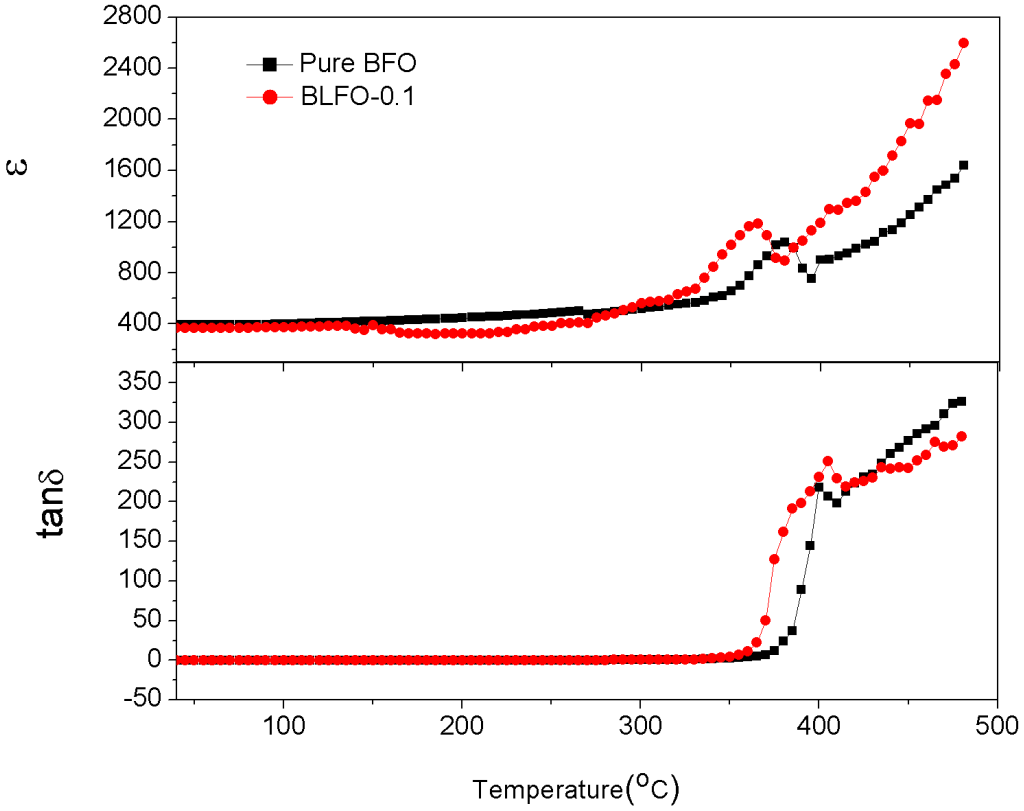

Fig. 4.8 The temperature dependence of dielectric constant (ε) and dielectric loss ($tan\delta$) at 10kHz of BFO and BLFO.

CHAPTER - 5

CONCLUSIONS:

Autocombustion technique is used to synthesize $BiFeO_3$ and La-doped $BiFeO_3$ ceramics. From the present study following conclusions can be drawn:

1. Structural analysis shows that La doping has reduced the impurity peak evident in undoped $BiFeO_3$ ceramics. The rhombohedral structure of parent compound is transformed to orthorhombic crystal structure. All the characteristic peaks were shifted to higher 2θ values showing a decrease in lattice parameters with an increase in La content.
2. The optical band gap values for undoped and doped $BiFeO_3$ nanoparticles have been calculated using UV-Vis absorption spectra. It shows that band gap of $BiFeO_3$ increases as the molar concentration of dopant increases. The calculated band gap values are 1.9080, 1.9980 and 2.0805 eV.
3. Room temperature dielectric properties show dispersion in dielectric constant and dielectric loss with frequency. High temperature dielectric measurements conform the magnetoelectric nature of BFO, with shifting of T_N towards room temperature. The dielectric constant is found to increase with increase in La content.

Thus we conclude that La-doped BFO is found to be a promising material for photo catalytic and dielectric applications.

REFERRENCES:

1. I.E. Dzyaloshinskii, Sov. Phys. JETP. **10**, 628 (1959).

2. D.N. Astrov, Sov. Phys. JETP. **11**, 708 (1909).

3. N. A. Spaldin, S. W. Cheong, R. Ramesh, Am. Inst. Phys., **10**, 38 (2010).

4. H. Schmid, J. Phys., Cond. Mat., **20**, 24 (2010).

5. E. Asher, H. Rieder, H. Schmid, H. Stossel, J. Appl. Phys.**37**,1404 (1966).

6. G. A. Smolenskii, I. E. Chupis, Sov. Phys. Usp. **25**, 475 (1982).

7. D. Khomskii, Am. Phyl. Soc. Phy., **2**, 20 (2009).

8. B. B. Van, Aken , T. T. M. Plastra, A. Filippetti, N. A. Spaldin, Nat. Mater., **3**, 164 (2004).

9. D. V. Efremov, J. van den Brink, D. I. Khomskii, Nat. Mater., **3**, 853 (2004).

10. S. W. Cheong, M. V. Mostovoy, Nat. Mater., **6**, 13 (2007).

11. T. Kimura, T. Goto, H. Shintani, K. Ishizaka, T. Arima, Y. Tokura, Nat. **426**, 55 (2003)

12. N. Hur, S. Park, P. A. Sharma, J. S. Ahn, S. Guha, S. W. Cheong, Nat. **429**,392 (2004).

13. T. Arima, J.Phys. Soc. Jpn., **76**, 073702 (2007).

14. Y. J. Choi, H. T. Yi, S. Lee, Q. Huang, V. Kiryukhin, and S.-W. Cheong Phys. Rev. Lett. **100**, 047601 (2008).

15. J. M. Moreau, C. Michel, R. Gerson, W. J. James, J. Phys. Chem. Solids, **32**, 1315 (1971).

16. V. S. Filipev, I. P. Smolyaninov, E .G Fesenko, I.I. Belyaev, Kristallografiya **5**, 958(1960), Sov. Phys. Crystallogr., **5**, 913 (1960).

17. F. Kubel, H. Schmid, Acta. Cryst. B, **46**, 698 (1990).

18. J. D. Bucci, B. K. Robertson, W. J. James, J. Appl. Cryst. **5**, 187 (1972).

19. M. I. Morozov, N. A. Lomanova, V. V. Gusarov, Russ. J. Gen. Chem., **73**, 1680 (2003).

20. M. Polomska, W. Kaczmarek, Z. Pajak, Phys. Stat. Sol., **23**,567 (1974).

21. S. Kamba, D. Nuzhnyy, M. Savinov, J. Sebek, J. Petzelt, J. Prokleska, R. Haumont, J. Kreisel, Phys. Rev. B, **75**, 024403 (2007).

22. W. Kaczmarek, Z. Pajak, M. Polomska, Solid State Commun., **17**, 807 (1975).

23. J .P. Rivera, H. Schmid, Ferroelectrics, **204**, 23 (1997).

24. J. R.Teague, R. Gerson, W. J. James, Solid State Commun. **8**, 1073 (1963).

25. a) D. Lebeugle, D. Colson, A. Forget, M. Viret, P. Bonville, J. F. Marucco, S. Fusil, Phys. Rev. B, 76, 024 116, (2007). b) D. Lebeugle, D. Colson , A. Forget, M. Viret, P. Bonville, J. F. Marucco, S . Fusil, Appl. Phys. Lett., **91**, 022 907 (2007).

26. J. Wang, J. B. Neaton, H. Zheng, V. Nagarajan, S. B. Ogale, B. Liu, D. Viehland, V. Vaithyanathan , D . G. Schlom, U. V. Waghmare, N. A. Spaldin , K. M. Rabe, M. Wuttig, R. Ramesh, Science, **299** , 1719 (2003).

27. a) J. Li, J. Wang, M. Wuttig, R. Ramesh, N. Wang, B. Ruette, A. P. Pyatakov, A. K. Zvezdin, D. Viehland, Appl. Phys. Lett., **84**, 5261 (2004) b) G. Xu, H. Hiraka, G. Shirane, J. Li, J. Wang, D. Viehland, Appl. Phys. Lett., **86**, 182905 (2005). c) S. Keisuke, K. Saito, A. Ulyanenkov, V. Grossmann, H. Ress, L. Bruegemann, H. Ohta, T. Kurosawa, S. Ueki, H. Funakubo, Jpn. J. Appl. Phys., **45**, 7311 (2006). d) G. Y. Xu, J. F. Li, D. Viehland, Appl. Phys. Lett., **89**, 222901 (2006).

28. D. Lebeugle, D. Colson, A. Forget, M. Viret, A. M. Bataille, A. Gukasov, Phys. Rev. Lett., **100**, 227602 (2008).

29. I. Sosnovska, T. Peterlin-Neumaier, E. Steichele, J. Phys. C, **15**, 4 835 (1982).

30. A. Palewicz, R. Przeniosło, I. Sosnowska, A. W. Hewat, Acta Cryst. B, **63**, 537 (2007).

31.T. P. Gujar, V. R. Shinde, C. D. Lokhande, Mater. Chem. Phys., **103**, 142 (2007).

32. S. M. Selbach, T. Tybell, M. A. Einarsrud, T. Grande, Chem. Mater., **19**, 6478 (2007).

33. T. J. Park, G. C. Papaefthymiou, A. J. Viescas, A. R. Moodenbaugh , S. S. Wong, Nano Lett., **7** , 766 (2006).

34. F. Gao, Y. Yuan, K. F. Wang, X. Y. Chen , F. C hen, J.-M. Liu, Z. F. Ren, Appl. Phys. Lett., **89**, 102506 (2006).

35. R. Mazumder, S. Ghosh, P. Mondal, D. Bhattacharya, S. Dasgupta, N. Das, A. Sen, A. K. Tyagi, M. Sivakumar, T. Takami, H. Ikuta, J. Appl. Phys., **100**, 033908 (2006).

36. a) J. T. Richardson, W. O. Milligan, Phys. Rev., 102, 1289, (1956). b) J. T. Richardson, D. I. Yiagas, B. Turk, K. Forster, M. V. Twigg, J. Appl. Phys., **70**, 6977 (1991).

37. T. J. Park, Y. B. Mao, S. S. Wong, Chem. Commun., 2708, (2004).

38. X. Y. Zhang, C. W. Lai, X. Zhao, D. Y. Wang, J. Y. Dai, Appl. Phys. Lett., **87**, 143102 (2005).

39. A.F. Junior, T.E.P. Alves, E.C.de.O. Lima, E. da S. Nunes, V. Zapf, Appl. Phys. A **94**,131–137 (2009).

40. J. Wang, J. B. Neaton, H. Zheng, V. Nagarajan, S. B. Ogale, B. Liu, D. Vieh-land, V. Vaithyanathan, D. G. Schlom, U. V. Waghmare, N. A. Spaldin, K. M. Rabe, M . Wuttig, R. Ramesh, Science, **299**, 5613, 1719 (2003).

41. Reetu, A. Agarwal, S. Sanghi, Ashima, N. Ahlawat, Monica, J. Appl. Phys. **111**, 113917 (2012).

42. D. Hong, S. Yu, J. Cheng, Currt. Appl. Phys. **11**, S255-S259 (2011).

43. C. Lan ,Y. Jiang ,Shaoguang, Yang, J. Mater. Sci **46**,734–738 (2011).

44. B. Ramachandran, Dixit, R. Naik,G. Lawes, M. S. Ramachandra Rao, J. Appl. Phys. **111**, 023910 (2012).

45. Amit Kumar, K.L. Yadav J. Phys. Chem. Solid, **72** ,1189–1194 (2011).

46. Q. Ke, X. Lou, Y. Wang, J. Wang, Phy. Rev. B, **82**, 024102 (2010).

47. D. P. Dutta,O. D. Jayakumar, A. K. Tyagi, K. G. Girija, C. G. S. Pillaiand G. Sharma, Nanoscale, **2** , 1149–1154 (2010).

48. J. Dhahri, M. Boudard, S. Zemni, H. Roussel, M. Oumezzine, J. Solid State Chem., **181**, 802 – 811 (2008).

49. Veis, E. Liskova, R. Anto , S .Visnovsky, Naresh Kumar, D.S. Misra, N. Venkataramani, S. Prasad, R. Krishnan, Thin Solid Film. **519**, 8041 – 8046 (2011).

50. C. Lan, Y. Jiang, S. Yang, J. Mater. Sci., **46**, 734–738 (2011).

51. M. Kumar, K. L. Yadav, G.D. Varma, Mater. Lett., **62**, 1159– 1161 (2008).

52. M. Y. Shami, M. S. Awan, M. Anis-ur-Rehman, J. Supercond. Nov. Magn., **26**, 1071–1074 (2013).

53. Z. X. Cheng, A. H. Li, X. L. Wang, S. X. Dou, K. Ozawa, H. Kimura, S. J. Zhang, T. R. Shrout, J. Appl. Phys. **103**, 07E507 (2008).

54. R. Das, K. Mandal, J. Magt. Mag. Mat., **324,** 1913–1918 (2012).

55. S. Mukherjee, S. Chakraborty, S. Mukherjee, Inter. J. Current Engg. Tech., **2**, 403 (2012).

56. G. S. Lotey, N.K. Verma, Supl. Microstr. **53**, 184–194 (2013).

57. S. C. Roy, G. L. Sharma, and M. C. Bhatnagar, Solid State Commun **141(5)**, 243-247 (2007).

58. A .Datta, A. Priyam, S. N. Bhattacharyya, K. K. Mukherjea, and A. Saha, J Colloid Interface Sci **322(1)**, 128–135 (2008).